J. Fluid Mech. (1999), *vol.* 388, *pp.* 389–409. Printed in the United Kingdom

Thermoacoustic heating and cooling in near-critical fluids in the presence of a thermal plume

By BERNARD ZAPPOLI[1,2], ARNAUD JOUNET[2], SAKIR AMIROUDINE[1] AND ABDELKADER MOJTABI[2]

[1] Centre National d'Etudes Spatiales, 18 Avenue Edouard Belin, 31405 Toulouse Cedex 04, France

[2] Institut de Mécanique des Fluides de Toulouse, UMR CNRS/INP-UPS 5502, LM2F, Université Paul Sabatier, 118 Route de Narbonne, 31062 Toulouse Cedex, France

(Received 11 August 1997 and in revised form 28 December 1998)

This work brings new insight to the question of heat transfer in near–critical fluids under Earth gravity conditions. The interplay between buoyant convection and thermoacoustic heat transfer (piston effect) is investigated in a two-dimensional non-insulated cavity containing a local heat source, to reproduce the conditions used in recent experiments. The results were obtained by means of a finite-volume numerical code solving the Navier–Stokes equations written for a low-heat-diffusing near-critical van der Waals fluid. They show that hydrodynamics greatly affects thermoacoustics in the vicinity of the upper thermostated wall, leading to a rather singular heat transfer mechanism. Heat losses through this wall govern a cooling piston effect. Thus, the thermal plume rising from the heat source triggers a strong enhancement of the cooling piston effect when it strikes the middle of the top boundary. During the spreading of the thermal plume, the cooling piston effect drives a rapid thermal quasi-equilibrium in the bulk fluid since it is further enhanced so as to balance the heating piston effect generated by the heat source. Then, homogeneous fluid heating is cancelled and the bulk temperature stops increasing. Moreover, diffusive and convective heat transfers into the bulk are very weak in such a low-heat-diffusing fluid. Thus, even though a steady state is not obtained owing to the strong and seemingly continuous instabilities present in the flow, the bulk temperature is expected to remain quasi-constant. Comparisons performed with a supercritical fluid at initial conditions further from the critical point show that this thermalization process is peculiar to near-critical fluids. Even enhanced by the thermal plume, the cooling piston effect does not balance the heating piston effect. Thus, overall piston-effect heating lasts much longer, while convection and diffusion progressively affect the thermal field much more significantly. Ultimately, a classical two-roll convective-diffusive structure is obtained in a perfect gas, without thermoacoustic heat transfer playing any role.

1. Introduction

A few years ago, investigations concerning the expected critical slowing down of thermal equilibration in convection-free near-critical fluids led instead to a new heat transfer mechanism being demonstrated to exist in those fluids. Under micro-gravity conditions, despite the vanishing heat diffusivity of the fluid, the temperature equilibration time was found to become increasingly shorter as the critical point was

approached. In 1990, three different teams (Zappoli *et al.*; Onuki, Hao & Ferrell; Boukari *et al.*) independently explained the 'critical speeding up' of the thermal equilibration observed in space-borne convection-free experiments. Further studies based on a global thermodynamic approach (Onuki & Ferrell 1990; Ferrell & Hao 1993), on the asymptotic analysis of the Navier–Stokes equations in the one-dimensional case (Zappoli 1992; Zappoli & Carlès 1995; Carlès 1995) or on their numerical resolution (Zappoli & Durand-Daubin 1994; Amiroudine *et al.* 1996; Amiroudine 1995), as well as new experimental works (Straub & Nitsche 1991, 1993; Guenoun *et al.* 1993; Bonetti *et al.* 1994; Boukari, Pego & Gammon 1995; Zhong & Meyer 1995; Fröhlich *et al.* 1996; Garrabos *et al.* 1998) brought novel insight into this mechanism, called the Piston Effect (PE). This phenomenon is essentially linked to the hypercompressibility and to the vanishing diffusivity of near-critical fluids. When near-critical fluids are locally heated in an enclosure, a thin thermal adaptative layer forms by diffusion. Owing to very high compressibility, the fluid located in the heated boundary layer strongly expands, compressing the rest of the fluid adiabatically. As a result, the temperature is homogeneously increased on a very short time scale compared to pure heat diffusion. The thermoacoustic nature of this effect (Spradley & Churchill 1975; Radhwan & Kassoy 1984) is now well established as well as its limits since it has been shown that all the heat brought to the wall of a container filled with a near-critical pure fluid could ultimately be transferred to the bulk at the speed of sound when approaching the critical point (Zappoli & Carlès 1996; Amiroudine *et al.* 1997).

If fast temperature equilibration is ensured by the PE in near-critical fluids, then the question that naturally arises is the origin of the strong convective flows observed on the ground: is the PE prevented by gravity, thus letting temperature and density gradients release the convective instabilities or is there something else? In a recent paper (Zappoli *et al.* 1996), the answer was given by means of numerical simulations. For this purpose, it was necessary to develop a two-dimensional unsteady numerical code able to simulate compressible low-Mach-number buoyant flows in hypercompressible and low-heat-diffusing fluids. This numerical challenge was successfully applied to a particular problem involving a near-critical fluid subjected, under normal gravity conditions, to heat addition at a vertical boundary of its square container. The authors first found that fluid thermalization was still achieved rapidly by the PE before natural convection had time to enhance heat transport. So, the origin of the strong convective instabilities in such a thermally quasi-homogeneous medium needed an extra explanation. In fact, when a small increase of the temperature is imposed at the boundary, the PE homogeneously heats the bulk fluid but a small part of the thermalization, concerning a few remaining percent of the temperature homogenization, is governed by diffusion and thus occurs on a much longer time scale (Onuki & Ferrell 1990; Zappoli 1992; Zappoli & Durand-Daubin 1994). In other words, temperature inhomogeneities are still present in the hot thermal boundary layer after the PE heating period. The huge associated density gradients trigger the observed strong convective flow. Mass equilibration is then initiated by the long-lasting quasi-isothermal convective motion.

More recently, measurements performed on the ground (D. Beysens 1995, private communication) led to new questions concerning the role of convection on the PE (Zappoli *et al.* 1996). As reported by Garrabos *et al.* (1998), some results showed that PE heating had not been detected in a near-critical fluid heated by a thermistor immersed in a thermally non-insulated cell. The question that was raised by these experiments was the origin of this quasi-absence of bulk heating. This was especially intriguing because convection-free microgravity experiments under the same heating conditions exhibited significant heating of the bulk. On the other hand, Zappoli

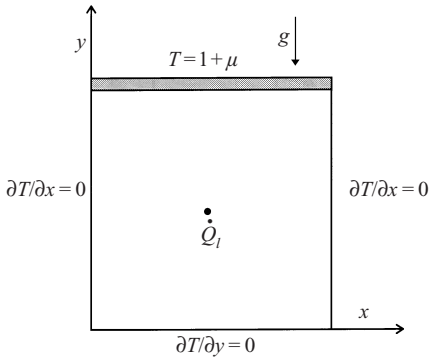

FIGURE 1. The centre-heated two-dimensional square cavity.

et al. (1996) have shown that the PE was not destroyed by convection in another heating configuration. Thus, something had to be clarified concerning the effects of the thermal boundary conditions and of the flow on the PE thermalization. In the present study, our numerical code is adapted to approach as far as possible the experimental configuration. Beside the explanation of the specific mechanism involved in this experiment, this paper sheds new light on the general question of heat transfer in near-critical fluids under 1 *g* conditions. Comparisons with the structure of the flow and the thermal field obtained for a normally compressible fluid (perfect gas) emphasize the present results. Even though buoyant convection in the near-critical fluid does not contribute directly to bulk heating, which remains driven by the PE, its interplay with diffusion in the 'cold' boundary layer formed at the top isothermal boundary, in which a cooling PE originates, is found to significantly accelerate thermal equilibrium in the bulk fluid. This equilibrium is found to result from a balance between the two competing PEs. Additional calculations show that this mechanism is not witnessed further from the critical point.

The model and the governing equations are presented in § 2, the numerical method in § 3 while § 4 is dedicated to the results and discussion.

2. The model and governing equations

2.1. *The model*

The following model is that developed by Zappoli (1992) and already used in previous papers (Zappoli & Durand-Daubin 1994; Zappoli & Carlès 1995, 1996; Zappoli *et al.* 1996).

We basically consider a two-dimensional square cavity filled with near-critical CO_2 under gravity. The heating source, located at the centre of the domain, provides constant power while all the boundaries are adiabatic, except the top wall which is maintained at constant temperature (see figure 1). The fluid is initially motionless, stratified around the critical density and at thermal equilibrium such that

$$\mu = \frac{T_i' - T_c'}{T_c'} \ll 1,$$

where T_i' and T_c' represent the initial and critical temperatures, respectively.

The supercritical fluid is considered to be a Newtonian, viscous and heat-diffusing fluid. Its motion is thus driven by the Navier–Stokes equations, coupled with the energy equation, while the van der Waals equation of state is chosen to describe its

thermodynamic behaviour. Even though this equation does not lead to the correct critical exponents (it exhibits a $(T' - T_c')^{-1}$ divergence of the compressibility and of the heat capacity at constant pressure, for example), it does permit phenomenologically correct investigations. Owing to its rather simple analytical form, relevant qualitative information on the processes occurring in near-critical fluids has already been obtained. The divergence of the thermal conductivity λ is taken into account separately by means of the relation

$$\lambda = \frac{\lambda'}{\lambda_0'} = 1 + \Lambda\left(\frac{T' - T_c'}{T_c'}\right)^{-1/2} \quad \text{(where } \Lambda = 0.75\text{)}$$

(throughout the paper, the prime denotes dimensional variables, the subscript 0 refers to the corresponding perfect gas value, and the subscript c to a critical value).

The variations of heat capacity at constant volume and dynamic viscosity are ignored, thus

$$C_v = \frac{C_v'}{C_{v0}{}'} = 1, \quad \tilde{\mu} = \frac{\mu'}{\mu_0'} = 1.$$

All these choices are consistent with previous analytical results, and thus make comparison between them and the present findings possible.

2.2. *Governing equations*

The conservation equations (mass, momentum, energy) and the equation of state for the Newtonian, viscous heat-conducting van der Waals fluid described above can be written as

$$\frac{\partial \rho}{\partial t} + \nabla \cdot (\rho \boldsymbol{v}) = 0, \tag{1}$$

$$\frac{\partial (\rho \boldsymbol{v})}{\partial t} + \nabla \cdot (\rho \boldsymbol{v} \otimes \boldsymbol{v}) = -\gamma_0^{-1} \nabla P + \varepsilon \left[\nabla^2 \boldsymbol{v} + \tfrac{1}{3} \nabla (\nabla \cdot \boldsymbol{v})\right] + \frac{1}{Fr_0} \rho \boldsymbol{g}, \tag{2}$$

$$\begin{aligned} \frac{\partial (\rho T)}{\partial t} + \nabla \cdot (\rho \boldsymbol{v} T) = & -(\gamma_0 - 1)(P + \tfrac{9}{8}\, \rho^2)(\nabla \cdot \boldsymbol{v}) \\ & + \frac{\varepsilon \gamma_0}{Pr_0} \nabla \cdot [\{1 + \Lambda (T-1)^{-0.5}\} \nabla T] \\ & + \varepsilon \gamma_0 (\gamma_0 - 1)\{v_{i,j} v_{j,i} + v_{i,j} v_{i,j} - \tfrac{2}{3} v_{i,i} v_{j,j}\} + r, \end{aligned} \tag{3}$$

$$P = \frac{\rho\ T}{1 - \rho/3}\ - \tfrac{9}{8} \rho^2. \tag{4}$$

In these equations, the following dimensionless dependent variables (density, temperature, presure and velocity) are defined:

$$\rho = \frac{\rho'}{\rho_c'}, \quad T = \frac{T'}{T_c'}, \quad P = \frac{P'}{\rho_c' R' T_c'}, \quad \boldsymbol{v} = \frac{\boldsymbol{v}'}{c_0'},$$

with the independent variables of space and time:

$$x = \frac{x'}{L'}, \quad y = \frac{y'}{L'}, \quad t = \frac{t'}{t_a'},$$

where ρ_c' and T_c' are the critical density (467.8 kg m^{-3}) and temperature (304.13 K), respectively; R' is the specific perfect gas constant for CO_2 (188.8 J kg^{-1} K^{-1}); $c_0{}' = (\gamma_0 R' T_c{}')^{1/2}$ is the perfect gas sound velocity, where γ_0 is the ratio of specific heats in

the reference state (1.4); $t_a' = L'/c_0'$ is the corresponding acoustic time, with L' the length of the cavity.

In equation (3), r simulates the heating source and is defined by

$$r = \frac{r'}{r_0'} \quad \text{with} \quad r_0' = \frac{\rho_c' R' T_c' c_0'}{L'(\gamma_0 - 1)};$$

r' denotes the power per unit volume injected by the thermistor. Therefore, $r' = \dot{Q}_l'/S_Q'$ at the centre of the cell, where $\dot{Q}_l'$ represents the heating rate per unit length ($0.74\,\mathrm{W\,m^{-1}}$ in our basic case) and S_Q' the section of the wire representing the thermistor.

In equations (2) and (3), ε is a small parameter defined by

$$\varepsilon = Pr_0 \frac{t_a'}{t_d'},$$

where t_d' refers to a diffusion characteristic time:

$$t_d' = \frac{L'^2}{\chi_0'}$$

(χ_0' denotes the thermal diffusivity at critical density for the ideal gas). This time represents the diffusion characteristic time for an ideal gas. Indeed, in a near-critical fluid, diffusion depends on the critical point proximity (through λ' and C_p', the heat capacity at constant pressure) and, as shown by Zappoli (1992) , its characteristic time is: $t_d'/\mu^{1/2}$, which is much longer than t_d'. For $L' = 10\,\mathrm{mm}$, $t_d' = 3.10^3\,\mathrm{s}$ and $t_a' = 35\ \mu\mathrm{s}$.

The additional symbols used above are Pr_0, the Prandtl number ($Pr_0 = \nu_0'/\chi_0'$, ν_0' the kinematic viscosity), and Fr_0, the Froude number ($Fr_0 = {c_0'}^2/L'g_0'$, with $g_0' = 9.8\ \mathrm{m\ s^{-2}}$) for an equivalent ideal gas. In our configuration, $Pr_0 = 2.27$ and $Fr_0 = 8.19 \times 10^5$.

All the conservation equations are written on the acoustic time scale. Since we are mainly interested in the PE and buoyant transports, a larger time scale is considered, defined by

$$\tau = \frac{\varepsilon f(\mu, \Lambda)}{\mu^2}\ t$$

with

$$f(\mu, \Lambda) = \mu\left(\frac{1}{\Lambda} + \frac{1}{\mu^{1/2}}\right).$$

Introduced by Zappoli (1992), it corresponds to the PE time scale in the linear one-dimensional case and remains quite suitable for our problem. A few K from T_c', it is shorter than the convective time scale and thus allows the flow to be correctly taken into account. The PE characteristic time ($t_{PE}' = t_a'\ \mu^2/\varepsilon f(\mu, \Lambda)$) is then also used for velocity normalization. Thus, on the PE time scale

$$\boldsymbol{v}_\tau = \frac{\mu^2}{\varepsilon f(\mu, \Lambda)} \boldsymbol{v}.$$

The stratified initial conditions close to the critical isochore can be written as

$$\left.\begin{aligned} &\boldsymbol{v} = 0, \quad T = 1 + \mu, \quad \rho(y) = \exp\left(-K(y-1)\right), \\ &P(y) = \tfrac{3}{2}(1+\mu) - \tfrac{9}{8} + \tfrac{9}{4}\mu \exp\left(-K(y-1)\right), \end{aligned}\right\} \tag{5}$$

with

$$K = \frac{4g\gamma_0}{9\mu Fr_0} \quad (g \text{ is the dimensionless gravity value}).$$

At the boundaries, the conditions are

$$\left.\begin{array}{l} \boldsymbol{v} = 0, \quad T = 1 + \mu \quad \text{at} \quad y = 1, \\ \partial T/\partial n = 0 \quad \text{on the other walls.} \end{array}\right\} \tag{6}$$

$\mu = 3.29 \times 10^{-3}$ if the initial temperature is set at 1K above T_c'.

The comparisons made with the perfect gas concern CO_2 in standard conditions, i.e. $T_0' = 300$ K and $\rho_0' = 1.8$ kg m^{-3}. The initial conditions are

$$\rho = 1, \quad T = 1, \quad P = 1, \quad \boldsymbol{v} = 0,$$

and the top boundary condition becomes

$$T(y = 1) = 1.$$

3. Numerical modelling

The numerical method used in our code is based on the finite-volume discretization method using the SIMPLER algorithm. The detailed development and discussion of these methods can be found in Patankar & Spalding (1972), Patankar (1980, 1985), Jang, Jelti & Acharya (1986), and Amiroudine *et al.* (1996, 1997). In order to avoid pressure oscillations, a staggered mesh has been developed where velocity components are defined on the sides of the cells and thermodynamic variables at the cell centres (Patankar 1980). The variable 'power-law' Cartesian mesh follows a geometrical series such that, in each region of the domain, one can refine the mesh in both directions. This is the case at the centre of the cell, where heat is injected, and close to the boundaries. But because of the low kinematic viscosity and the low thermal duffusivity of the near-critical fluid, a large density of points was also required all over the domain. The discretization schemes tested in the calculations are the Power-Law scheme, introduced by Patankar (1980) from the exponential scheme, and the QUICK scheme proposed by Hayase, Humphrey & Greif (1992). Since the mesh has been strongly refined in many cases, the contribution of numerical diffusion effects was found not to influence the solution significantly (Leonard & Drummond 1995). Our code has been carefully tested against some relevant benchmark cases (Amiroudine 1995, Amiroudine *et al.* 1996, 1997). For all the results presented in this paper, we made sure of the validity of the solutions by testing the time step and the grid spacings, through the number of grid points or through the refining exponents of the mesh.

Beside these general methods, the acoustic-filtering procedure has been utilized (Paolucci 1982). For small-Mach-number compressible flows, as is currently the case, it is possible to reduce the computation times by means of this method when an acoustic-wave description is not needed. For explicit methods, this permits the time step to be increased since stability criteria are no longer governed by acoustic phenomena, which are removed from the equations. From implicit schemes making use of relaxation procedures, the gain is derived from the increase of the convergence rate since the relaxation of long-wavelength errors for the calculation of the overall pressure is a slow process in the low-Mach-number range (Paolucci).

Acoustic filtering consists of the following procedure. The dependent variables are

expanded in terms of the small Mach number (Ma):

$$\boldsymbol{v} = Ma\ (\boldsymbol{v}^{(0)} + Ma^2\boldsymbol{v}^{(1)} + o\ (Ma^2)),$$

$$T = T^{(0)} + Ma^2 T^{(1)} + o\ (Ma^2),$$

$$P = P^{(0)} + Ma^2 P^{(1)} + o\ (Ma^2),$$

$$\rho = \rho^{(0)} + Ma^2\rho^{(1)} + o\ (Ma^2).$$

When substituted in the Navier–Stokes equations, this leads to $P^{(0)} = P^{(0)}(t)$, i.e. the first term in the pressure expansion is spatially uniform, and the contribution of the pressure to the momentum equation is $O(Ma^2)$. $P^{(0)}$ accounts for the change of the static pressure with time while $P^{(1)}$ accounts for the hydrostatic and dynamic effects. Using the PE time scale for the definition of the reference velocity:

$$U' = \frac{\varepsilon f(\mu, \Lambda)}{\mu^2}\ c_0'$$

the dimensionless second-order pressure is given by

$$P^{(1)} = \frac{P^{(1)'}}{\rho_c' U'^2}.$$

The additional unknown resulting from the pressure splitting requires one more equation. The static pressure $P^{(0)}(t)$ is calculated by means of total mass conservation at each time step:

$$\int_V \rho \mathrm{d}V = \int_V \rho_i \mathrm{d}V$$

(where ρ_i refers to the initial value of the density).

4. Results and discussion

The model described in §§2 and 3 is considered for the study of the thermal behaviour of near-critical CO_2 contained in a two-dimensional square cavity and subjected to gravity and to a local constant power injection of $0.74\,\mathrm{W\,m^{-1}}$. This value was chosen to fit experimental data. For the small experimental cylindrical cell used by Beysens *et al.*, it is approximately equivalent to 5 mW, i.e. strong heating. Initially, the fluid is set at 1 K above the critical temperature and is slightly stratified around the critical density. All the boundaries are insulated, excepted the top wall which is kept at the initial temperature (figure 1). Some calculations with other thermal boundary conditions and gravity levels, or for fluid at different initial conditions, are however considered so as to clarify the analysis. A 200×200 point grid was used near the CP. The coarsest mesh was utilized for the perfect gas (70×70).

4.1. *The flow and thermal field*

Because of the large thermal dilation and low diffusivity of the fluid, steep density gradients (about $5 \times 10^4\,\mathrm{kg\,m^{-4}}$) appear close to the heat source, the temperature of which only increases approximately up to 2 K above the initial temperature. Consequently, the buoyancy force generates a strong flow (velocity reaches $15\,\mathrm{mm\,s^{-1}}$), and a thermal plume rises to the top wall as was observed experimentally (Bonetti *et al.* 1994; Garrabos *et al.* 1998). The main flow features can be seen in figure 2, which represents the velocity field at different times. The hydrodynamics look very

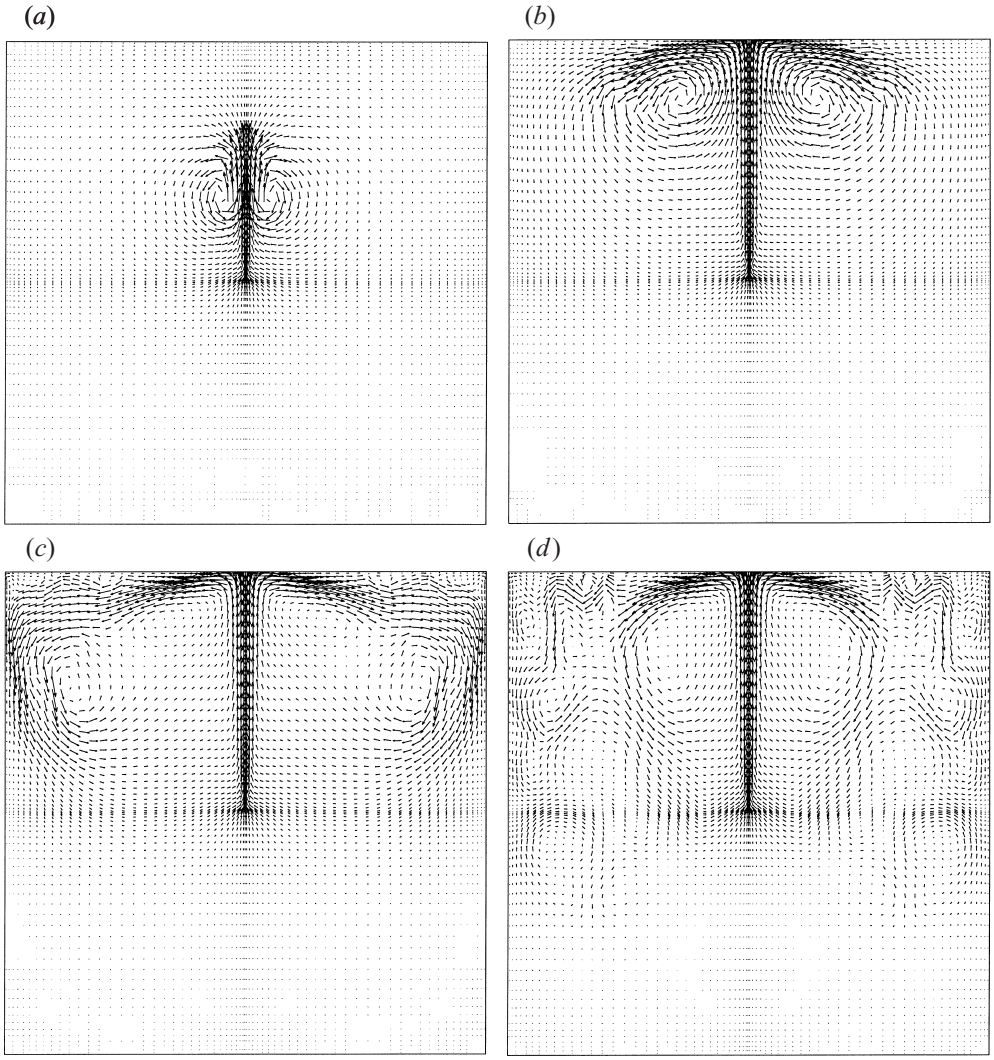

FIGURE 2. Velocity field at (*a*) $t' = 0.48$ s, (*b*) 1.19 s, (*c*) 2.38 s and (*d*) 4.76 s.

complicated and highly nonlinear because of the anomalous behaviour of many properties near the critical point (Gitterman 1978). Two contrarotating cells form beside the front of the rising flow by viscous coupling (figure 2*a*). Then, the plume strikes the top boundary (figure 2*b*) and spreads along the thermostated wall (figure 2*c*) in a very transient way. The flow becomes complex with secondary vortices appearing (figure 2*d*). On the other hand, the lower part of the cavity is weakly affected by convection. The temperature distribution in the fluid during the same period is represented in figure 3(*a–d*). For $t' = 0.48$ s, 1.19 s, 2.38 s and 4.76 *s*, the isothermal lines are plotted for temperature elevations varying from $\Delta T' = 0$ to $\Delta T' = 30$ mK. The poorness of diffusive heat transfer is clearly exhibited. Figure 3(*a*) shows that the very local vortices contribute to extracting some heat from the rising flow. Otherwise, the presence of a thermal adaptative layer along the top thermostated wall shows that the bulk fluid temperature has undergone a homogeneous rise: since neither convection nor diffusion from the heat source can have brought any heat

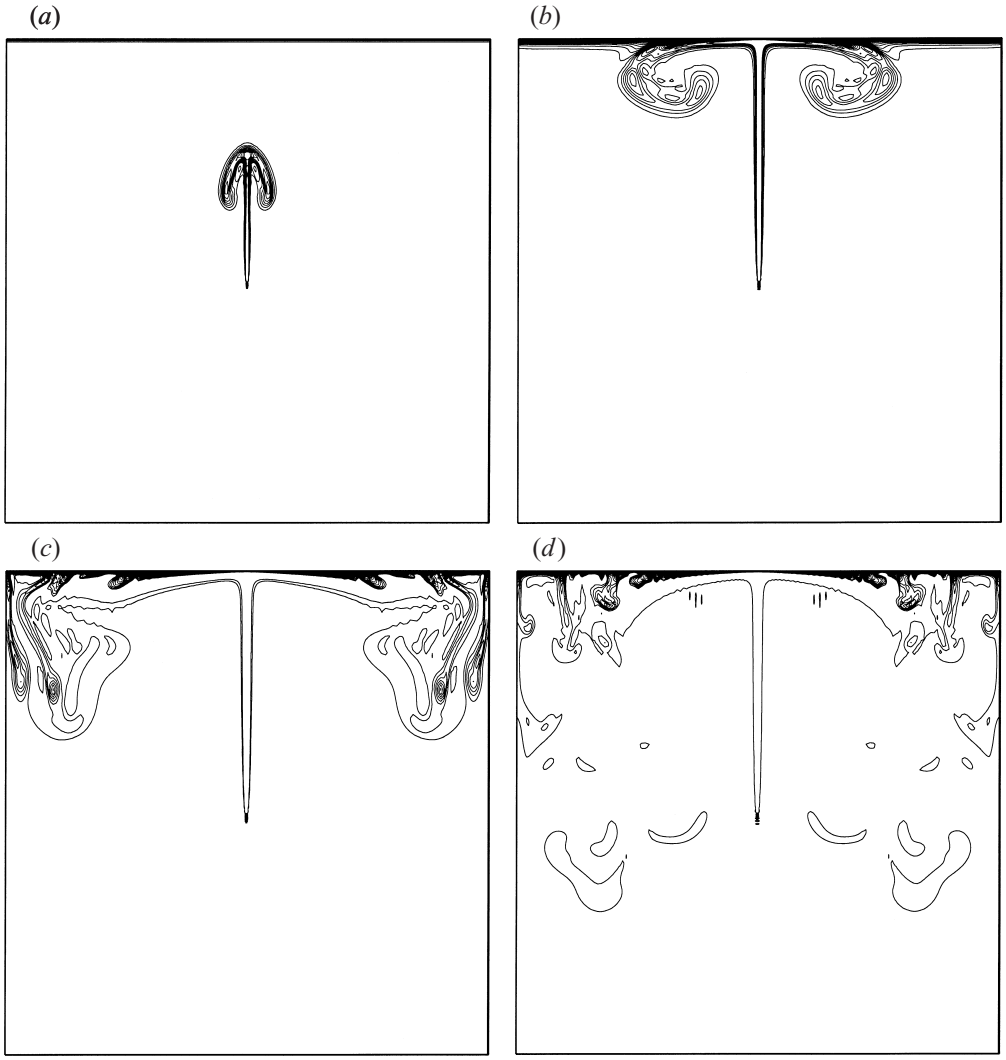

FIGURE 3. Thermal field at (*a*) $t' = 0.48$ s, (*b*) 1.19 s, (*c*) 2.38 s and (*d*) 4.76 s.

into this area, this is the stamp of the PE, which is still efficient in the presence of convection. The thermal field in the upper part of the cavity exhibits a complex structure as soon as the plume strikes the wall (figure 3*b–d*). The area of interaction between the cold boundary layer (CBL) and the warm plume is progressively extended. In addition to the flow linked to the spread of the thermal plume, some cooler (and consequently heavier) masses of fluid, like drops, tend to escape down from the CBL, while two warmer masses of fluid ejected out of the plume by buoyancy during spreading, like bubbles, are convected up to the CBL, leading to new changes in its pattern (figure 3*c*). These figures also show that only the small portion of fluid located in the core of the plume is significantly warmer than the bulk fluid. This means that diffusive convection cannot transport a lot of heat into the bulk. This can be seen as early as $t' = 0.48$ s in figure 4, which represents the temperature elevation profile from the thermistor to the top boundary. The strong decrease corresponds to the convective transport and ends with $\Delta T' \sim 40$ mK in the front propagating

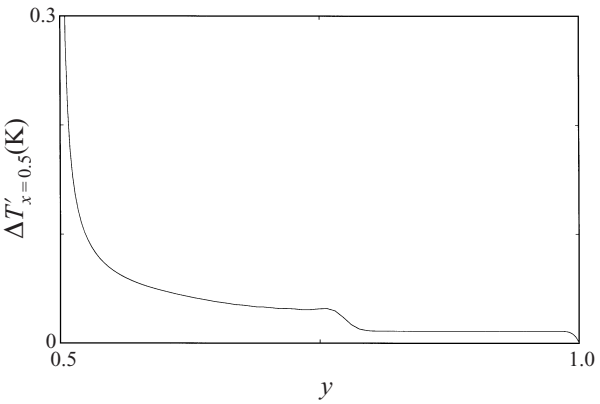

FIGURE 4. Temperature elevation profile at $x = 0.5$ and $t' = 0.48$ s from $y = 0.5$ (thermistor) to $y = 1$ (top thermostated wall).

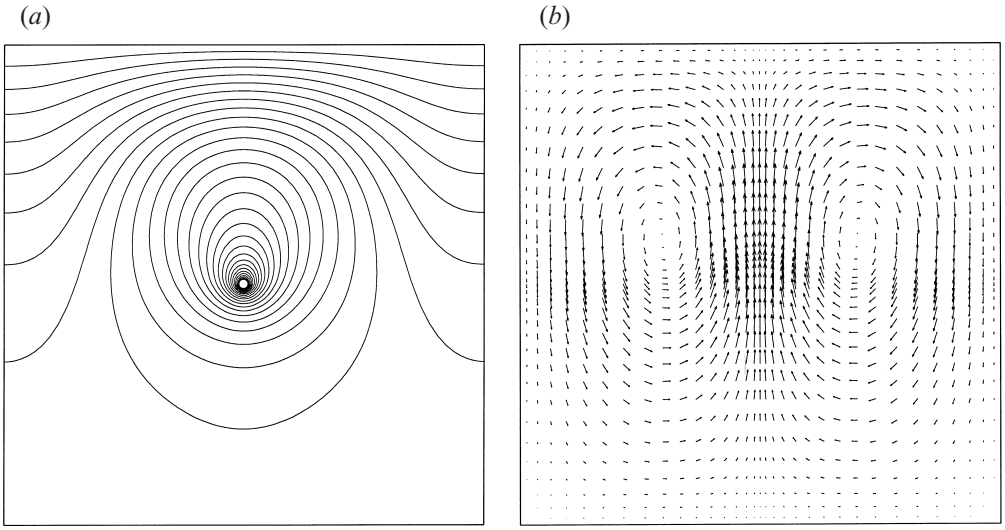

FIGURE 5. (*a*) Thermal and (*b*) velocity field at $t' = 4.76$ s for the perfect gas.

flow, which is followed (as y increases) by a constant value exhibiting homogeneous heating by PE, and then by the CBL diffusive profile.

Until $t' = 4.76$ s, all these plots exhibit that the PE alone causes bulk thermalization in near-critical CO_2, since neither convection nor diffusion carries away a lot of heat.

4.2. *Comparison with the perfect gas*

The results of the same calculation for normally compressible (perfect gas) CO_2 are completely different. The temperature map (figure 5*a*), plotted at $t' = 4.76$ s (heat and mass transport is almost steady at this time), exhibits classical convective–diffusive transport. Heat diffuses in the whole cavity and the PE does not have any influence. The flow field represented in figure 5(*b*) is also very different from that of the near-critical fluid. Since the density is about 250 times smaller, kinematic viscosity is greatly increased and the whole fluid becomes involved in a two-roll structure. The specificity of the hydrodynamics at near-critical conditions is also emphasized in figure 6 by the comparison of the velocity profiles along the vertical axis at $x = 0.5$ and $t' = 4.76$ s

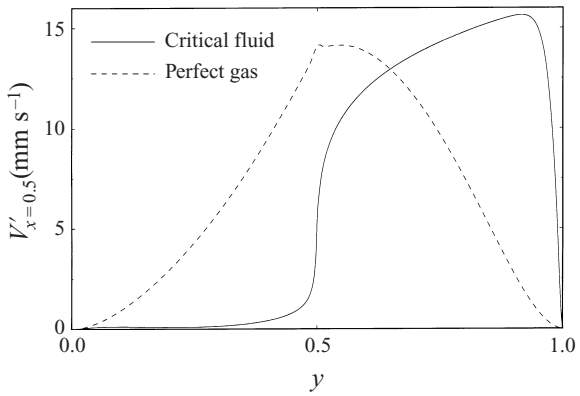

FIGURE 6. Vertical velocity profile at $x = 0.5$ and $t' = 4.76$ s for the supercritical fluid and the perfect gas.

(in the near-critical fluid, the flow is almost steady here at this time). For $y < 0.5$, one can observe that the supercritical fluid is little affected by buoyant convection (which originates at the heat source located at $y = 0.5$) compared with the perfect gas. On the contrary, the flow is continuously speeded up for $y > 0.5$ in the critical fluid, up to near the top wall, while it is slowed down in the perfect gas because the presence of the top wall is taken into account much further from it. This is an indication that convection can significantly affect thermal diffusion much closer to the thermostated boundary in near-critical conditions.

It is also interesting to note that the maximum velocity has the same order of magnitude in the two cases. Zappoli *et al.* (1996) found that the velocity induced in the perfect gas was much lower than that of the near-critical fluid, but their heat source came from an increase of the left-hand boundary temperature while in the present configuration, a local heat flux is imposed. Consequently, the temperature of the fluid in contact with the heat source here reaches more than 70 K in the perfect gas. This value is much higher than for the near-critical fluid (2 K) because the heat capacity at constant pressure is lower, and it induces large density gradients too ($\sim 100\,\mathrm{kg\,m^{-4}}$). Thus, even though such gradients are smaller than those present in critical CO_2, since the fluid in normal conditions is about 250 times less dense, it is not surprising that the buoyant force generates a flow of comparable intensity.

4.3. *Piston effect thermalization*

In the near-critical fluid, the results presented above show that thermalization is achieved by the PE. But it must be recalled that, since a CBL forms at the thermostated wall, a cooling PE (CPE) is linked with the contraction of the fluid affected by the wall's cooling, so that the global PE results from competition between the heating PE (HPE) born from the expansion of the fluid located in the thermistor hot boundary layer (HBL) and the CPE, as pointed out in a previous analytical work (Zappoli & Carlès 1995). In order to illustrate the CBL significance in terms of PE, figure 7 plots the vertical velocity and the temperature profiles (marked with triangles), close to the top wall at $x = 0.75$ and $t' = 6$ ms (before natural convection becomes dominant in this area). Solid lines correspond to the current configuration while dashed lines represent the results of the same computation when the upper boundary is adiabatic. In the presence of the CBL, a dynamic boundary layer appears simultaneously. When cooled in the CBL, the fluid strongly contracts and induces the motion of the rest

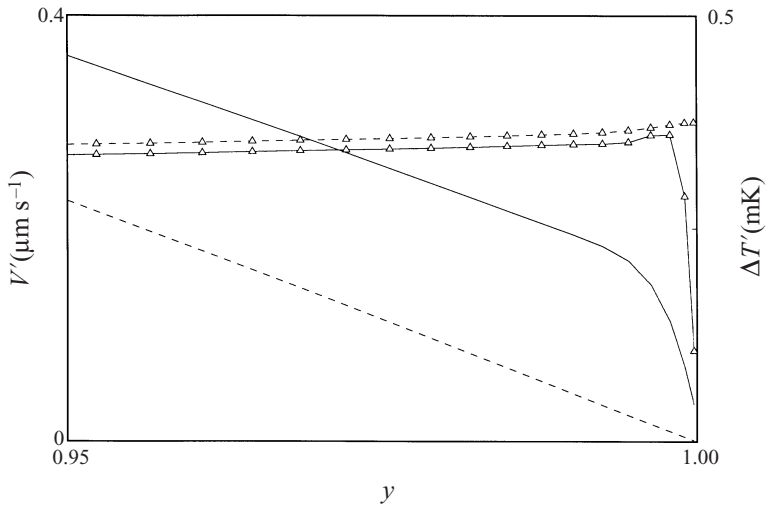

FIGURE 7. Vertical velocity and temperature elevation (triangles) profiles versus y at $x = 0.75$ and $t' = 6$ ms close to the top wall when it is thermostated (solid line) or insulated (dashed line).

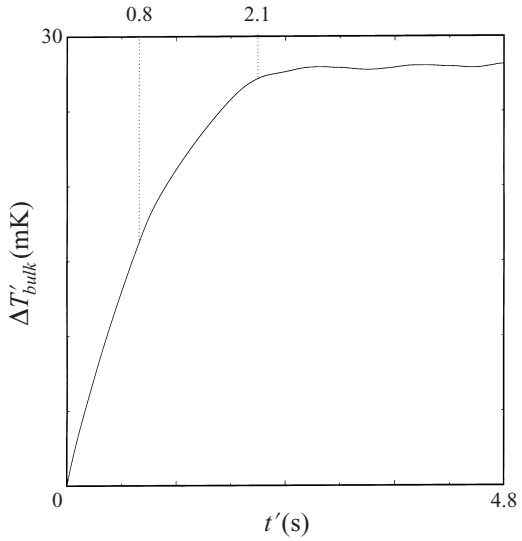

FIGURE 8. Temperature elevation versus time at $(x, y) = (0.25,0.25)$ for $g = 1$ and a thermostated upper wall.

of the fluid toward the top wall. The bulk velocity is increased compared to the case in which it only results from HBL expansion (dashed line), and mass flow occurs towards the CBL. Consequently, the bulk density is lower (pressure is decreased) and the bulk temperature too. This can be observed in figure 7: homogeneous cooling is added, in the bulk, to heating caused by the HPE, corresponding to the presence of expansion waves generated at the edge of the CBL (Zappoli & Carlès 1995).

For the problem under investigation, global PE heating in the fluid is shown in figure 8, which reports the bulk temperature variations with time. They are measured at a location where neither convection nor diffusion carries any significant amount of heat, in the bulk of the bottom part of the cavity for example. Two inflection

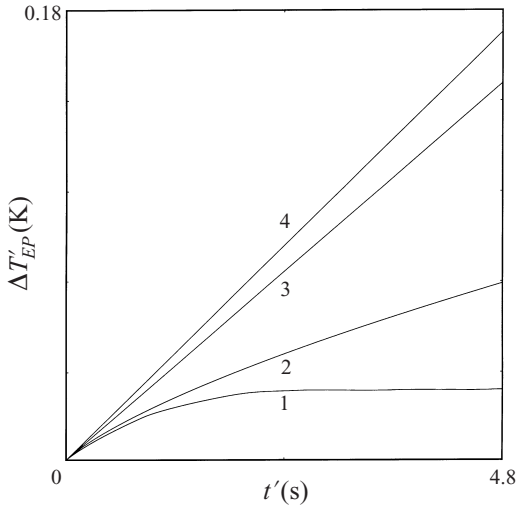

FIGURE 9. Bulk temperature variations: for $g = 1$ and a thermostated upper wall (curve 1), for $g = 0$ and a thermostated upper wall (curve 2), for $g = 1$ and insulated boundaries (curve 3), for $g = 0$ and insulated boundaries (curve 4).

points during the temperature increase can be clearly distinguished: first around $t' = 0.8$ s and then around $t' = 2.1$ s, that finally lead to a quasi-constant value (28 mK). This means that PE heating stops early, as reported by D. Beysens (private communication). This bulk temperature variation is completely different from that observed for $g = 0$, the simulation of which is plotted in figure 9 (curve 2, to be compared with curve 1, which represents the plot of figure 8) and which exhibits a continuous increase. This experimentally observed difference is, of course, linked to convection but the exact mechanism of this interaction has yet to be determined.

4.4. *Effect of convection on the heating piston effect*

First, in order to suppress the CPE and isolate the role of natural convection on the HPE alone, we performed the calculations with the upper boundary being thermally insulated. The results are reported in figure 9 for $g = 1$ (curve 3) and $g = 0$ (curve 4). It appears that the temperature increase for $g = 1$ is slightly lower than for $g = 0$, indicating that the HPE is only slightly affected by convection. This result is consistent with what has already been found for the side-heated cavity (Zappoli *et al.* 1996), even though the PE seemed to be stronger in that study when $g = 1$.

Otherwise, these plots show that the thermal response of the bulk fluid to the PE is proportional to the heat flux at the heating edge, as theoretically discussed by Zappoli & Carlès (1995) in a one-dimensional asymptotic analysis. The bulk density variations also follow a linear increase versus time (not plotted). Then, the ratio of the internal energy variations caused by the PE with respect to the heat brought by the thermistor is calculated as 27%. This is in good agreement with the $\frac{1}{4}$ theoretical value (for a van der Waals gas). Comments on this energy efficiency can be found in Garrabos *et al.* (1998), for instance. The important point in the discussion that follows is this proportionality between the heating flux and the homogeneous PE temperature increase versus time.

It is why Zappoli *et al.* (1996) found that PE heating was slightly enhanced in the presence of convection. Indeed, in their study, the heat source was provided by a fixed

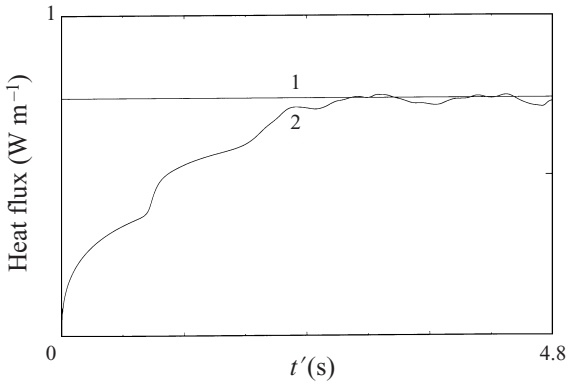

FIGURE 10. Heat fluxes injected by the thermistor (curve 1) and lost at the upper wall (curve 2) versus time.

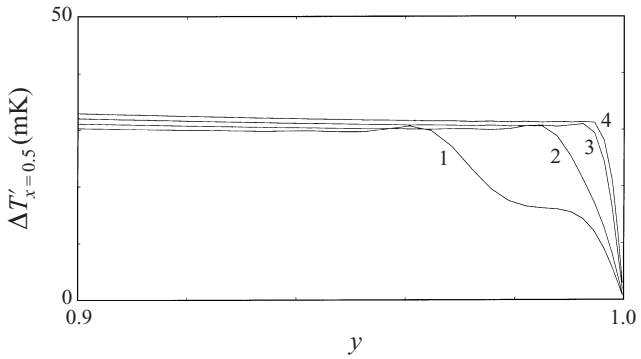

FIGURE 11. Temperature profiles around the cold boundary layer when the rising plume begins to strike the wall (at $x = 0.5$) for different times: $t' = 0.76$ s (curve 1), $t' = 0.81$ s (curve 2), $t' = 0.86$ s (curve 3), $t' = 0.91$ s (curve 4).

increase of the temperature on one side of the cavity. Under 1 g conditions, buoyant convection along this vertical wall enhanced temperature gradients in the HBL by hindering the diffusion of this thermal layer. Thus, the decrease of the HPE efficiency pointed out in curves 3 and 4 was overcome by the enhancement of the heat flux received by the fluid located in the HBL.

4.5. *Thermoacoustic cooling triggered by the thermal plume*

Now, let us come back to curve 1 (figure 9). Since it appears that the HPE is not greatly affected by convection, the changes in bulk fluid heating in comparison with the situation in weightlessness (curve 2) are necessarily linked to CPE modifications. This is also suggested by the plot in figure 10, which represents the total heat fluxes at the boundaries as a function of time, in curve 1 for the thermistor (constant) and in curve 2 for the cold wall. Indeed, the PE heating rate variations are perfectly correlated to the variations of the heat flux at the thermostated boundary. The overall bulk heating rate is found to be directly proportional to the total heat flux and is thus governed by the fluctuations of heat losses. These fluctuations are connected to hydrodynamic events near the CBL, as shown in the following discussion.

In figure 9, the small difference between curves 1 and 2 until $t' \sim 0.8$ s is similar to that observed between curves 3 and 4. On the other hand, the inflection point in the

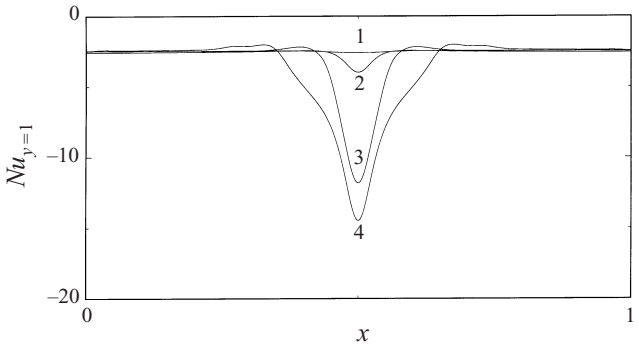

FIGURE 12. Nusselt number at the upper wall for different times: $t' = 0.71$ s (curve 1), $t' = 0.81$ s (curve 2), $t' = 0.91$ s (curve 3), $t' = 1.19$ s (curve 4).

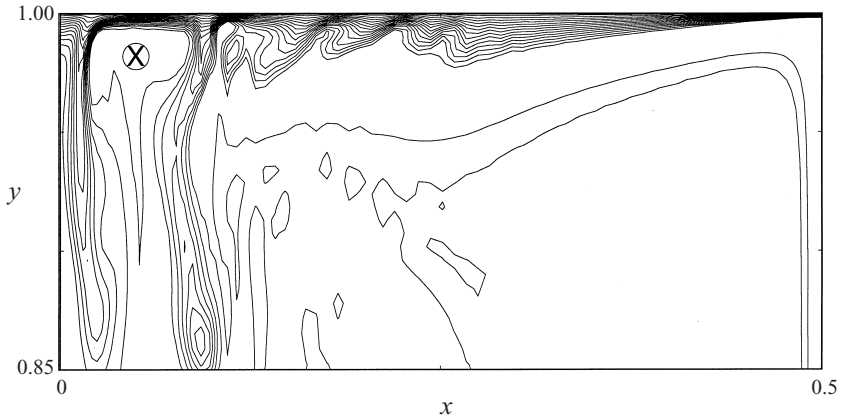

FIGURE 13. Thermal field at $t' = 2.19$ s close to the cold boundary layer.

heating slope occurring at $t' \sim 0.8$ s must be due to CPE enhancement. At this time, the rising plume reaches the middle of the upper wall and the structure of the CBL becomes locally considerably modified. Figure 11 shows the variations caused by this flow between $t' = 0.76$ s and $t' = 0.91$ s: the outer boundary layer temperature becomes that of the flow and the thermal diffusing layer is made suddenly much thinner. This leads to much steeper temperature gradients in this region of the CBL and to a sudden enhancement of heat losses through the thermostated wall, as shown by curve 2 in figure 10. Then, the fluid located in the CBL is submitted to stronger cooling from the isothermal wall. Hence, it contracts more; the CPE is enhanced and global PE heating decreases (figure 8). The Nusselt number at the top boundary plotted versus x at different moments in figure 12 also illustrates these sudden changes of the CBL thermal structure. At $t' = 1.2$ s (curve 4), heat loss increases in the middle of the wall slow down, and it can be seen that they become smaller further from this area because of the flow spreading toward the sides of the cavity (see also figures 2*b* and 3*b*). Thus, another crucial event must occur to explain the second significant deviation of the heating rate at $t' \sim 2.1$ s (figure 8). In fact, the CBL is again submitted to sudden local modifications of its structure at this moment. Figure 13, which represents the thermal field in the upper left side of the cavity (the flow is symmetrical over the

central vertical axis), shows that a 'bubble-like structure' of warm fluid impinges on each corner of the wall. Some masses of warm fluid convected by the plume have escaped from the two vortices because of their buoyancy and strike both sides of the isothermal wall around $t' = 2.1$ s. Heat losses are consequently increased (see figure 10), and the CPE is enhanced again (figure 8).

In addition, it is interesting to observe the complexity of the CBL in this region. Because of the large density gradients that may occur in such a hypercompressible fluid, the CBL seems to be affected by gravitational instabilities. These instabilities seem to result primarily from Rayleigh–Taylor-like instabilities. As a matter of fact, a diffusive layer in miscible liquids or in a one-phase supercritical fluid has been recently shown to behave like an interface in which diffusivity plays a similar role to that played by surface tension in a real equilibrium interface (Kurowski, Misbah & Tchourkine 1995; Zappoli, Amiroudine & Gauthier 1997). However, in the present configuration, a flow perpendicular to the density gradients and the two impinging 'quasi-bubbles' seem to interact with this instability. Further investigations are clearly needed to fully identify the mechanism which drives the CBL evolution.

4.6. *Thermal quasi-equilibrium on the piston effect time scale and long-term behaviour*

After $t' \sim 2.4$ s, figures 8 and 10 show that bulk heating stops when the boundary heat fluxes balance each other. This means that CPE cooling has become strong enough to balance the heating caused by the HPE, because of the convection-forced heat diffusion at the cold wall. Consequently, a state of thermal quasi-equilibrium is reached in the bulk fluid. The global PE transports some energy from the HBL to the CBL without any bulk heating, since all the heat brought to the bulk by the HPE is instantaneously retrieved by the homogeneous cooling caused by the CPE. In such conditions, the bulk fluid behaviour can be compared to that of a thermal short-circuit, the state of which is insensitive to the energy transferred through it.

Figures 3(*c*) and 3(*d*) show that convection transports very little heat into the bulk between $t' = 2.4$ s and $t' = 4.8$ s. Neither heat brought by the thermal plume nor the small heavier masses of fluid escaping down from the CBL generate significant variations around the equilibrium temperature in the bulk fluid. The weak bulk temperature oscillations after $t' = 2.4$ s (figure 8) are linked to the CBL instabilities, since they provoke heat loss fluctuations (figure 10). It can be inferred that this behaviour should be maintained after $t' = 4.8$ s. Indeed, figure 2(*d*) shows that, on each side of the plume, which remains structured only on the middle of the upper part of the cavity, the flow has become very unsteady from the top corners to the lower part of the cavity, and could even be turbulent. Thus, no steady state is expected. On the other hand, this flow does not significantly affect the thermal quasi-equilibrium over long periods of time since the temperature of the fluid it transports is close to the equilibrium temperature.

In weightlessness, thermalization would then obey a completely different process. For the sake of clarity, this is shown in figure 14, which results from one-dimensional simulations with the same heating. PE heating in the bulk increases continuously while diffusion becomes more and more significant over longer time scales. Furthermore, a steady state should be reached on the diffusion time scale when heat losses balance the imposed heating; a purely conductive temperature profile is expected. In the presence of buoyancy, convection has two major effects on the fluid thermal response: first, thermal equilibrium between the HPE and the CPE is reached very soon in the bulk; secondly, thermal diffusion is hindered and does not significantly affect thermalization for long.

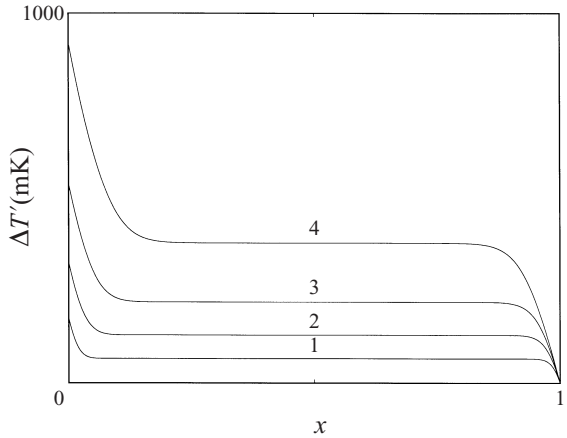

FIGURE 14. Temperature profiles in one dimension with $P' = 74$ W m^{-2}, at $t' = 4.76$ s (1), $t' = 11.9$ s (2), $t' = 23.8$ s (3) and $t' = 47.6$ s (4).

Figure 14 also shows that PE heating contributes more to the increase of the temperature gradients in the CBL than diffusion contributes to their decrease. This means that the CPE is increased by PE heating. This was already suggested by the increasing difference between curves 2 and 4 in figure 9 (weightlessness), which showed that the CPE became increasingly efficient versus time. In fact, the HPE and the CPE naturally tend to equilibrium with such boundary conditions; when diffusion is prevented by convection near the CBL, this tendency is even stronger and acts concurrently with the blind CPE enhancement triggered by convection. This must be mentioned to emphasize that the balance between the two PEs arising in the presence of convection does not result from a particular value of the injected power, or from a specific convective enhancement of heat losses. Global PE heating makes the CPE stronger and thus, global heating less efficient. On the other hand, if the CPE becomes stronger than the HPE, the global PE cools; it contributes to decreasing the temperature gradients in the CBL and weakens the CPE. Through the CPE fluctuations, the CBL responds like a damper to any PE heating or cooling, and like a spring to any disturbance of the balance between heat fluxes. Thus, heat flux at the cold wall is driven by two factors in the present configuration: convection, which enhances it greatly, and the CPE, which permits a balance to be reached. The last parameter driving heat losses is the thermal conductivity of the fluid, which only depends on the proximity of the system to the critical point.

4.7. *Further from the critical point*

The thermal behaviour observed above is linked to critical point proximity. This is illustrated by the simulation performed with the fluid initially at $T'_i = T'_c + 15$ K and $\rho'_i = \rho'_c + 125$ kg m^{-3}.

The temperature maps plotted in figures 15(*a*) and 15(*b*) at $t' = 7.14$ s and $t' = 19$ s, in which isotherms vary from $\Delta T' = 0$ to $\Delta T' = 300$ mK, show that diffusive convection has greater effects on fluid thermalization (see also figure 16). It seems here that diffusion drives heat transport over long periods of time, since the lower part of the cavity becomes affected from $t' = 7.14$ s to $t' = 19$ s. Actually, thermal diffusivity increases due to the larger distance from the critical point, but the temperature of the fluid heated by the thermistor is also larger, and convection transports much

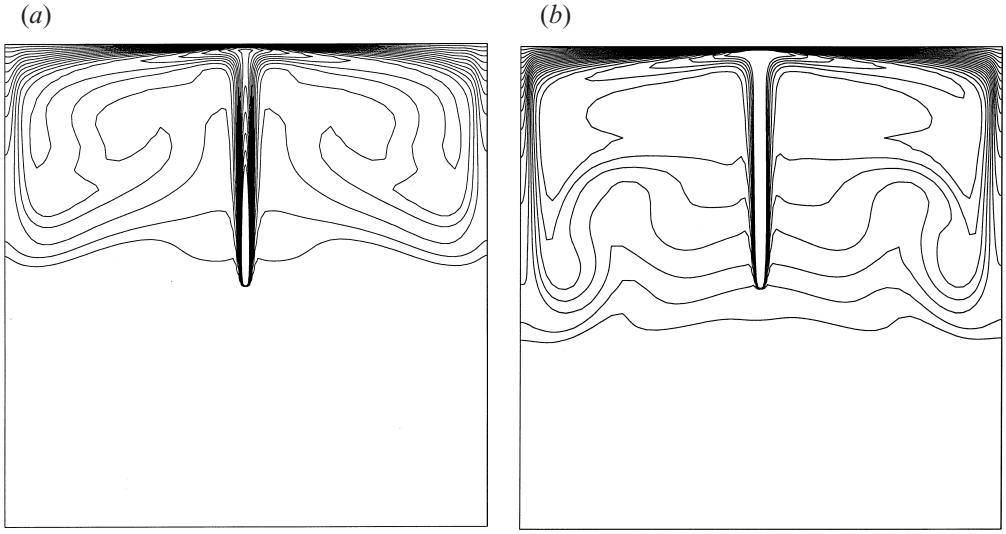

FIGURE 15. Thermal field at (*a*) $t' = 7.14$ s and (*b*) $t' = 19$ s for $T'_i = T'_c + 15$ K and $\rho'_i = \rho'_c + 125$ kg m^{-3}.

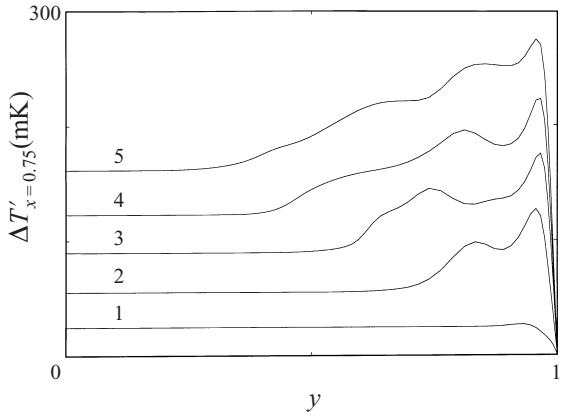

FIGURE 16. Temperature profiles at $x = 0.75$ for $t' = 1.19$ s (1), $t' = 3.57$ s (2), $t' = 7.14$ s (3), $t' = 11.9$ s (4) and $t' = 23.8$ s (5) for $T'_i = T'_c + 15$ K and $\rho'_i = \rho'_c + 125$ kg m^{-3}.

more heat. On the other hand, figures 16 and 17 (curves 1 and 2) show that the PE is still efficient and greatly contributes to fluid heating until $t' = 23.8$ s. These plots also illustrate that overall PE heating continues after the plume has spread along the upper thermostated wall (around $t' = 2$ s). Since thermal conductivity is lower at 15 K above the critical point, heat flux through this wall is weaker, while injected power is the same as previously (see curves 3 and 4 in figure 17). Thus, the HPE remains stronger than the CPE over longer times. In addition, note that there seems to be no gravitational instability in the CBL: this phenomenon is associated with the extent of the density gradients in this area, which are found to be about 10 times lower in the present conditions. Then, a real steady state might be reached if the flow transience is not continuously supplied. Nevertheless, figure 17 shows that this state is still far from being reached at $t' = 23.8$ s.

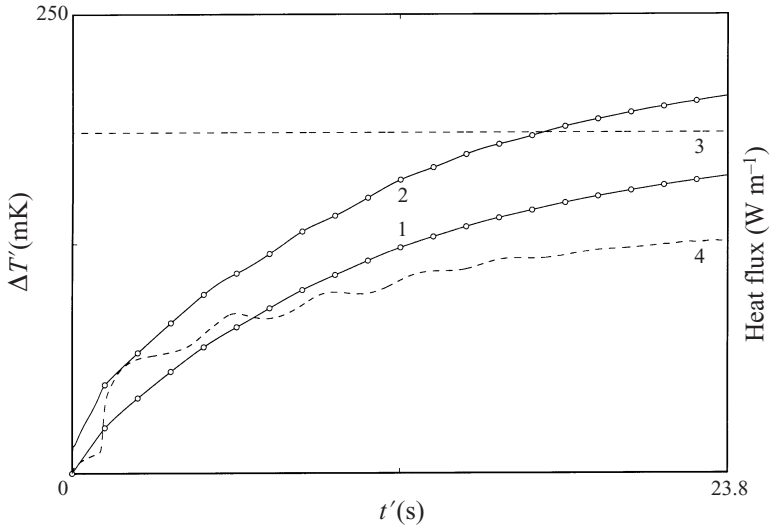

FIGURE 17. For $T_i' = T_c' + 15\,\mathrm{K}$ and $\rho_i' = \rho_c' + 125\,\mathrm{kg\,m^{-3}}$, temperature elevation versus time: bulk value (1) and mean value (2); dashed lines: heat fluxes injected by the thermistor (3) and lost at the upper wall (4).

Finally, when moving away from the critical point, the computation shows that thermal quasi-equilibrium in the bulk no longer exists. Since compressibility is still high, the PE contributes significantly to fluid thermalization, but the CPE becomes weaker because thermal conductivity decreases. Diffusive transport increases and should characterize the final temperature map.

5. Conclusion

The aim of this study was to identify a new heat transfer mechanism in near-critical fluids, which was suspected to exist according to recent experiments conducted on the ground and in micro-gravity. The response of a near-critical fluid confined in a non-insulated cavity submitted to strong internal heating in the presence of buoyancy has been analysed by means of the numerical simulation of the Navier–Stokes equations written for a van der Waals low-heat-diffusing fluid. Thermalization is still found to be governed by the piston effect, even though piston-effect heating ends very soon. An important coupling between the piston effect and convection is found to occur through modifications of the heat losses at the upper thermostated boundary, which drive a cooling piston effect. Because of the low kinematic viscosity of the near-critical fluid, the buoyant flow greatly affects the topology of the temperature field along the thermostated wall. The consequence is a modification of the balance between the heating and cooling piston effects responsible for the strong difference in the bulk temperature observed in experiments conducted either under Earth gravity conditions or under zero gravity. The early end to heating thus results from the enhancement of the cooling piston effect and not from a destructive interaction between convection and thermoacoustic effects. Over longer times, the thermal quasi-equilibrium in the bulk fluid should be maintained since convective and diffusive heat transfers are very weak.

This particular thermalization process is shown to be specific to near-critical fluids. Indeed, further from the critical point, thermal conductivity is smaller and even when the plume has impinged upon the thermostated wall, heat losses are not sufficiently

high to balance the injected flux. Concurrently, thermal diffusion is stronger and drives a significant part of fluid heating. A true steady state should be reached in such conditions. This is not expected close to the critical point, particularly because of the strong instabilities near the cold boundary layer.

This work is a further step in the identification of new heat transfer mechanisms in near-critical fluids. However, some new features are reported that concern hydrodynamics of dense hypercompressible low-heat-diffusing fluids and need further investigation. In the near future, this research will be developed in two directions: to characterize the boundary layer instabilities and their relations with thermoacoustic effects; and to introduce a real equation of state to perform quantitative comparisons with experiments.

The authors acknowledge Dr Yves Garrabos for interesting discussions and comments.

REFERENCES

Amiroudine, S. 1995 Modélisation numérique des phénomènes de transport de chaleur et de masse dans les fluides supercritiques. PhD thesis, Institut de Mécanique des Fluides de Marseille, France.

Amiroudine, S., Larroudé, Ph., Bontoux, P. & Zappoli, B. 1996 Numerical simulations of convective instabilities in near-critical pure fluids. *Proc. Second Eur. Symp. In Space, Napoli* (*Italy*).

Amiroudine, S., Ouazzani, J., Zappoli, B. & Carlès, P. 1997 Numerical solutions of 1D unsteady hypercompressible flows using finite volume methods. *Eur. J. Mech.* B **16**, 665.

Bonetti, M., Perrot, F., Beysens, D. & Garrabos, Y. 1994 Fast thermalization in supercritical fluids. *Phys. Rev.* E **49**, 4779.

Boukari, H., Pego, R. L. & Gammon, R.W. 1995 Calculation of the dynamics of gravity-induced density profiles near a liquid-vapor critical point. *Phys. Rev.* E **52**, 1614.

Boukari, H., Shaumeyer, J. N., Briggs, M. E. & Gammon, R.W. 1990 Critical speeding up in pure fluids. *Phys. Rev.* A **41**, 2260.

Carlès P. 1995 Etude de l'effet piston et des phénomènes thermo-acoustiques dans les fluides supercritiques. PhD thesis, Institut National Polytechnique de Toulouse, France.

Ferrell, R. A. & Hao, H. 1993 Adiabatic temperature changes in a single-component fluid near the liquid-vapor critical point. *Physica* A **197**, 23–46.

Fröhlich, T., Guenoun, P., Bonetti, M., Perrot, F., Beysens, D., Garrabos, Y., Le Neindre, B. & Bravais, P. 1996 Adiabatic versus conductive heat transfer in off-critical SF_6 in the absence of convection. *Phys. Rev.* **54**, 1544.

Garrabos, Y., Bonetti, M., Beysens, D., Perrot, F., Fröhlich, T., Carlès, P. & Zappoli, B. 1998 Relaxation of a supercritical fluid after a heat pulse in the absence of gravity effects: Theory and experiments. *Phys. Rev.* E **57**, 1.

Gitterman, M. 1978 Hydrodynamics of fluids near a critical point. *Rev. Mod. Phys.* **50**, 85.

Guenoun, P., Beysens, D., Khalil, B., Garrabos, Y., Kammoun, B., Le Neindre, B. & Zappoli, B. 1993 A thermocycle around the critical point of CO_2 under reduced gravity. *Phys. Rev.* E **47**, 1531.

Hayase, T., Humphrey, J. A. C. & Greif, R. 1992 A consistently formulated QUICK scheme for fast and stable convergence using finite-volume iterative calculation procedures. *J. Comput. Phys.* **98**, 108.

Jang, D. S., Jelti, R. & Acharya, S. 1986 Comparison of the PISO, SIMPLER and SIMPLEC algorithms for the treatment of the pressure-velocity coupling in steady flow problems. *Numer. Heat Transfer* **10**, 209.

Kurowski, P., Misbah, C. & Tchourkine, S. 1995 Gravitational instability of a fictitious front during mixing of miscible fluids. *Eur. Phys. Lett.* **29**, 309.

Leonard, B. P. & Drummond, J. E. 1995 Why you should not use 'Hybrid', 'Power-Law' or related exponential schemes for convective modelling–There are much better alternatives. *Intl J. Numer. Meth. Fluids* **20**, 421.

Onuki, A. & Ferrell, R. A. 1990 Adiabatic heating effect near the gas-liquid critical point. *Physica* D **164**, 245.

Onuki, A., Hao, H. & Ferrell, R. A. 1990 Fast adiabatic equilibrium in a single component fluid near the liquid-vapor critical point. *Phys. Rev.* A **41**, 2256.

Paolucci, S. 1982 On the filtering of sound from the Navier–Stokes equations. *SAND* 82-8257.

Patankar, S. V. 1980 *Numerical Heat Transfer and Fluid Flow*. Hemisphere.

Patankar, S. V. 1985 A calculation procedure for two-dimensionnal elliptic situations. *Numer. Heat Transfer* **14**, 409.

Patankar, S. V. & Spalding, D. P. 1972 A calculation procedure for heat, mass and momentum transfer in three-dimensional parabolic flows. *Intl J. Heat Mass Transfer* **15**, 1787.

Radhwan, A. M. & Kassoy, D. R. 1984 The response of a confined gas to a thermal disturbance: rapid boundary heating. *J. Engng Maths* **18**, 133.

Spradley, L. W. & Churchill, S. W. 1975 Pressure- and buoyancy-driven thermal convection in a rectangular enclosure. *J. Fluid Mech.* **70**, 705.

Straub, J. & Nitsche, K. 1991 In *Proc. 11th Symp. on Thermophysical Properties, Boulder, Colorado*.

Straub, J. & Nitsche, K. 1993 Isochoric heat capacity C_v at the critical point of SF_6 under micro and earth-gravity. Results of the German spacelab mission D_1. *Fluid Phase Equil.* **88**, 183.

Zappoli, B. 1992 The response of a nearly supercritical pure fluid to a thermal disturbance. *Phys. Fluids* A **4**, 1040.

Zappoli, B., Amiroudine, S., Carlès, P. & Ouazzani, J. 1996 Thermoacoustic and Buoyancy-driven transport in a square side heated cavity filled with a near critical fluid. *J. Fluid Mech.* **316**, 53.

Zappoli, B., Amiroudine, S. & Gauthier, S. 1997 Presented at the *13th Symp. on Thermophysical Properties, Boulder, Colorado*.

Zappoli, B., Bailly, D., Garrabos, Y., Le Neindre, B., Guenoun, P. & Beysens, D. 1990 Anomalous heat transport by the piston-effect in supercritical fluids under zero gravity. *Phys. Rev.* A **41**, 2264.

Zappoli, B. & Carlès, P. 1995 Thermoacoustic nature of the critical speeding-up. *Eur. J. Mech.* B **14**, 41.

Zappoli, B. & Carlès, P. 1996 Acoustic saturation of the critical speeding-up. *Physica* D **89**, 381.

Zappoli, B. & Durand-Daubin, A. 1994 Direct numerical modelling of heat and mass transport in a nearly supercritical fluid. *Phys. Fluids* **6**, 1929.

Zhong, F. & Meyer, H. 1995 Density equilibration near the liquid-vapor critical point of a pure fluid: single phase $T > T_c$. *Phys. Rev.* E **51**, 3223.